The Astrophysical Journal, 968:102 (12pp), 2024 June 20 https://doi.org/10.3847/1538-4357/ad4607

Electron Heating in the Transrelativistic Perpendicular Shocks of Tilted Accretion Flows

Lorenzo Sironi[1,2] and Aaron Tran[1,3]

[1] Department of Astronomy and Columbia Astrophysics Laboratory, Columbia University, 550 W 120th St. MC 5246, New York, NY 10027, USA; lsironi@astro.columbia.edu, atran@physics.wisc.edu

[2] Center for Computational Astrophysics, Flatiron Institute, 162 5th Ave., New York, NY 10010, USA

[3] Department of Physics, University of Wisconsin–Madison, 1150 University Ave., Madison, WI 53706, USA

Received 2024 February 20; revised 2024 March 26; accepted 2024 April 25; published 2024 June 17

Abstract

General relativistic magnetohydrodynamic (GRMHD) simulations of black hole tilted disks—where the angular momentum of the accretion flow at large distances is misaligned with respect to the black hole spin—commonly display standing shocks within a few to tens of gravitational radii from the black hole. In GRMHD simulations of geometrically thick, optically thin accretion flows, applicable to low-luminosity sources like Sgr A* and M87*, the shocks have transrelativistic speed, moderate plasma beta (the ratio of ion thermal pressure to magnetic pressure is $\beta_{\rm pi1} \sim 1$–8), and low sonic Mach number (the ratio of shock speed to sound speed is $M_s \sim 1$–6). We study such shocks with 2D particle-in-cell simulations, and we quantify the efficiency and mechanisms of electron heating for the special case of preshock magnetic fields perpendicular to the shock direction of propagation. We find that the postshock electron temperature $T_{\rm e2}$ exceeds the adiabatic expectation $T_{\rm e2,ad}$ by an amount $T_{\rm e2}/T_{\rm e2,ad} - 1 \simeq 0.0016 M_s^{3.6}$, nearly independent of the plasma beta and of the preshock electron-to-ion temperature ratio $T_{\rm e1}/T_{\rm i1}$, which we vary from 0.1 to unity. We investigate the heating physics for $M_s \sim 5$–6 and find that electron superadiabatic heating is governed by magnetic pumping at $T_{\rm e1}/T_{\rm i1} = 1$, whereas heating by B-parallel electric fields (i.e., parallel to the local magnetic field) dominates at $T_{\rm e1}/T_{\rm i1} = 0.1$. Our results provide physically motivated subgrid prescriptions for electron heating at the collisionless shocks seen in GRMHD simulations of black hole accretion flows.

Unified Astronomy Thesaurus concepts: Galaxy accretion disks (562); Stellar accretion disks (1579); Shocks (2086); Plasma astrophysics (1261)

Supporting material: machine-readable table

1. Introduction

Electrons emit the light we see from accreting black holes, including the famed Event Horizon Telescope (EHT) images of M87* and Sagittarius A* (Sgr A*) (Event Horizon Telescope Collaboration et al. 2019, 2022a). Yet, the electron temperature in such systems, and hence the source of their luminosity, is uncertain. In low-luminosity sources like Sgr A* and M87*, the density in the hot, geometrically thick accretion flow is so low that the plasma is nearly collisionless. Therefore, wave-particle interactions regulate the energy exchange between protons and electrons. In recent years, analytical models and plasma simulations have been used to study the efficiency of electron heating. It is generally assumed that energy dissipation is governed either by magnetic reconnection (Rowan et al. 2017, 2019) or by plasma turbulence (e.g., Howes 2010; Arzamasskiy et al. 2019, 2023; Kawazura et al. 2019; Zhdankin et al. 2019; Kawazura et al. 2020; Zhdankin 2021; Comisso & Sironi 2022; Squire et al. 2023). Physically motivated inputs for the electron heating rate can then be incorporated into general relativistic magnetohydrodynamic (GRMHD) simulations and used to produce synthetic images and spectra to compare with observations.

In recent years, GRMHD simulations of "tilted" disks—where the angular momentum of the accretion flow at large distances is misaligned with respect to the black hole spin—have shown that shocks form within a few to tens of gravitational radii from the black hole (Fragile et al. 2001, 2007; Fragile & Blaes 2008; Dexter & Fragile 2011, 2013; McKinney et al. 2013; Morales Teixeira et al. 2014; Zhuravlev et al. 2014; White et al. 2019, 2020; Tsokaros et al. 2022; White & Quataert 2022; Bollimpalli et al. 2023, 2024; Chatterjee et al. 2023; Kaaz et al. 2023; Liska et al. 2023; Musoke et al. 2023; Ressler et al. 2023), in agreement with earlier analytical arguments (e.g., Ogilvie 1999; Ogilvie & Latter 2013; Fairbairn & Ogilvie 2021). Tilted disks are of general interest because (1) the accretion disk around Sgr A* could be tilted within EHT constraints (Event Horizon Telescope Collaboration et al. 2022b), and (2) dynamics within tilted disks may help explain the time-varying emission from Sgr A* or the mysterious quasiperiodic oscillations (QPOs) of galactic X-ray binaries (XRBs). In weakly collisional tilted disks (as well as in aligned disks, see Conroy et al. 2023), shocks then offer a novel channel for energy dissipation and electron heating—in addition to reconnection and turbulence. It is therefore timely to assess if, and how much, proton energy can be transferred to electrons at collisionless shocks for the conditions expected in tilted accretion flows.

In this paper, we use 2D particle-in-cell (PIC) simulations to quantify the efficiency and mechanisms of electron heating for the special case of preshock magnetic fields perpendicular to the shock direction of propagation. We are primarily motivated by the shock conditions extracted by Generozov et al. (2014) from the GRMHD simulation by Fragile et al. (2007) of a radiatively inefficient, geometrically thick accretion flow. These shocks have transrelativistic speed (the shock-frame upstream Lorentz factor is ∼1.2–1.8), moderate ion beta $\beta_{\mathrm{pi}1} \sim 1$–8 (the ratio of ion pressure to magnetic pressure), and low sonic Mach number $M_s \sim 1$–6 (the ratio of shock speed to sound speed). Both the shock velocity and the Mach number increase for larger tilt angles (compare Figures 6 and 7 in Generozov et al. 2014). While extensive literature exists on electron heating in nonrelativistic shocks (e.g., Raymond et al. 2023), the plasma conditions most relevant for collisionless shocks in tilted accretion disks are still unexplored. The regime of low sonic Mach number and moderate-to-high plasma beta is similar to the case of merger shocks in galaxy clusters studied by Guo et al. (2017, 2018), yet the flow velocity in black hole disks is much faster than in the intracluster medium, and the study of such shocks deserves a separate investigation.

This paper is organized as follows. We describe the setup of our PIC simulations in Section 2, and present the general structure of the shocks in Section 3. In Section 4, we discuss the physics of electron heating and show that the postshock electron temperature $T_{\mathrm{e}2}$ exceeds the adiabatic expectation $T_{\mathrm{e}2,\mathrm{ad}}$ by approximately $T_{\mathrm{e}2}/T_{\mathrm{e}2,\mathrm{ad}} - 1 \simeq 0.0016 M_s^{3.6}$, nearly independent of the plasma beta and of the preshock ion-to-electron temperature ratio $T_{\mathrm{e}1}/T_{\mathrm{i}1}$, which we vary from 0.1 to unity. As we discuss in Section 5, this fitting formula can be used to incorporate the electron shock-heating physics into GRMHD simulations of tilted accretion disks.

2. Simulation Setup

We simulate 2D ion–electron shocks using the relativistic particle-in-cell (PIC) code TRISTAN-MP (Buneman 1993; Spitkovsky 2005). Our shocks are formed by reflecting a leftward traveling flow off a stationary wall at $x = 0$; the shock travels from left to right along $+\hat{x}$. The simulation (lab) frame is the downstream rest frame. Plasma is injected from the right-side x boundary, which continuously recedes from the wall to remain ahead of the shock at all times. The y boundary is periodic.

Subscript 0 refers to upstream quantities measured in the simulation frame. Subscript 1 refers to upstream quantities measured in the upstream rest frame. Subscript 2 refers to downstream quantities measured in the downstream rest frame (which coincides with the simulation frame). An exception is made for the 3-velocities v_1, v_2 and the 4-velocities u_1, u_2 (where $u_1 = v_1/\sqrt{1-(v_1/c)^2}$, and similarly for u_2), which are measured in the shock frame.

The upstream flow is a drifting ion–electron plasma with 3-velocity v_0 (Lorentz factor $\gamma_0 = 1/\sqrt{1-(v_0/c)^2}$), single-species density n_0, and magnetic field B_0 in the simulation frame. The upstream magnetic field has an angle $\theta_{Bn0} = 90°$ with respect to the $\hat{x}$-direction of the shock normal, and it lies along the y-direction (in Guo et al. 2017, we demonstrated that this in-plane geometry is most suitable for studying electron heating in low Mach number shocks, as compared to the alternative case of out-of-plane fields oriented along z). Ions are singly charged, and the plasma is charge neutral. We employ the realistic mass ratio $m_{\mathrm{i}}/m_{\mathrm{e}} = 1836$. The rest-frame single-species upstream density is $n_1 = n_0/\gamma_0$. Both ions and electrons are Maxwell–Jüttner distributed with initial temperatures $T_{\mathrm{i}1}$ and $T_{\mathrm{e}1}$ respectively. The dimensionless temperature is $\theta_{s1} = k_{\mathrm{B}} T_{s1}/(m_{s1} c^2)$, where subscript $s \in \{\mathrm{i}, \mathrm{e}\}$ indicates particle species.

The relative balance of rest-mass, thermal, magnetic, and kinetic energies in the upstream plasma is fully specified by dimensionless ratios. The ion dimensionless temperature $\theta_{\mathrm{i}1}$ specifies the relative balance of thermal and rest-mass energy. Motivated by GRMHD simulations, we fix $\theta_{\mathrm{i}1} = 0.01$. The upstream ion plasma beta $\beta_{\mathrm{pi}1} = 8\pi P_{\mathrm{i}1}/B_1^2$ is the ratio between the ion thermal pressure and the magnetic pressure, which we vary in the range $1 \leqslant \beta_{\mathrm{pi}1} \leqslant 8$. The ratio between kinetic and thermal energies is set by the sonic Mach number $M_{\mathrm{s}} = v_1/c_{s1}$, where the upstream sound speed $c_{s1} = \sqrt{(\Gamma_{\mathrm{i}}\theta_{\mathrm{i}1} + \Gamma_{\mathrm{e}}\theta_{\mathrm{e}1} m_{\mathrm{e}}/m_{\mathrm{i}}) c^2/h}$ with $\Gamma_{\mathrm{i}} = 5/3$, $\Gamma_{\mathrm{e}} = 4/3$, and specific enthalpy $h \approx 1 + 5\theta_{\mathrm{i}1}/2 + 4\theta_{\mathrm{e}1} m_{\mathrm{e}}/m_{\mathrm{i}}$ for nonrelativistic ions and relativistic electrons (equivalently, one could use the Alfvénic Mach number or the magnetosonic Mach number). Since we set up our simulation in the downstream rest frame, we cannot choose M_s directly; instead, we control the simulation-frame, ion-sound Mach number $M_{0\mathrm{i}} = v_0/c_{\mathrm{si}1}$ with $c_{\mathrm{si}1} = \sqrt{\Gamma_{\mathrm{i}}\theta_{\mathrm{i}1} c^2}$, and we measure M_s after the simulation ends. We explore the dependence of electron heating on $M_{0\mathrm{i}}$, which varies from 2 to 5.

In the absence of efficient collisional coupling, ions and electrons might have different temperatures ahead of the shock. In most models of low-luminosity accretion flows (Sgr A*, M87*), electrons need to be a factor of 3–10 colder than ions in order to explain the observed spectrum (e.g., Narayan & Yi 1995; Yuan et al. 2003). The two-temperature nature of the gas in low-luminosity accretion flows is a generic prediction because (i) electrons radiate much more efficiently than ions, (ii) coupling between ions and electrons via Coulomb collisions is inefficient at the low densities expected in the innermost regions, and (iii) compressive heating favors nonrelativistic ions over relativistic electrons. In this work, we vary $T_{\mathrm{e}1}/T_{\mathrm{i}1}$ from 0.1 to 1. For our chosen $\theta_{\mathrm{i}1} = 0.01$, the dimensionless electron temperature in the upstream varies in the range $\theta_{\mathrm{e}1} = 1.84$–18.4. The resulting sonic Mach number M_s varies from 2.6 to 6.1. For $T_{\mathrm{e}1}/T_{\mathrm{i}1} = 1$, the ratio $M_s/M_{0\mathrm{i}} \sim 0.9$ to 1.3; for $T_{\mathrm{e}1}/T_{\mathrm{i}1} = 0.1$, the ratio $M_s/M_{0\mathrm{i}} \sim 1.2$ to 1.6.

We define reference plasma scales and parameters based on the upstream flow properties. We initialize the preshock medium with 16 particles per cell per species in the simulation frame. The plasma frequency is $\omega_{\mathrm{ps}} = \sqrt{4\pi n_1 e^2/m_{\mathrm{s}}}$ and the plasma skin depth is $d_{\mathrm{s}} = c/\omega_{\mathrm{ps}}$. The transverse width of the domain in the y-direction is $22.4\, d_{\mathrm{i}}$. We resolve the electron skin depth d_{e} with three cells. For our choice of $\theta_{\mathrm{i}1} = 0.01$ and $T_{\mathrm{e}1}/T_{\mathrm{i}1} \geqslant 0.1$, the electron dimensionless temperature is $\theta_{\mathrm{e}1} \geqslant 1.8$, so the electron Debye length $\lambda_{\mathrm{De}} = \sqrt{k_{\mathrm{B}} T_{\mathrm{e}1}/(4\pi n_1 e^2)}$ is always well resolved. We measure time in units of the inverse ion cyclotron frequency defined with lab-frame quantities, $\Omega_{\mathrm{i}} = eB_0/(m_{\mathrm{i}} c)$, and length in units of the ion Larmor radius $\rho_{\mathrm{i}} = \gamma_0 v_0 m_{\mathrm{i}} c/(eB_0)$ (still defined with lab-frame quantities). It is not obvious whether lab-frame quantities are the most appropriate to use in our definitions of time and length units. Nevertheless, our definitions suffice up to order-unity corrections.

We compute the Mach number M_s as follows. At the end of the simulations ($\Omega_{\mathrm{i}} t \sim 25$ for all cases apart from $\beta_{\mathrm{pi}1} = 1$, where we evolve until $\Omega_{\mathrm{i}} t \sim 40$), we identify the lab-frame shock position x_{shock} as the right-most ion density peak. We then estimate the shock-frame flow velocities as $v_2 = x_{\mathrm{shock}}/t$ and $v_1 = (v_0 + v_2)/(1 - v_0 v_2/c^2)$, which yield a measurement of $M_s = v_1/c_{s1}$.

Our ion plasma beta sweep targeted four points, $\beta_{\mathrm{pi}1} \approx 1$, 2, 4, 8; the actual values of $\beta_{\mathrm{pi}1}$ vary by up to 10% between simulations (Table 1). Of particular note, the $M_{0\mathrm{i}} \approx 5$ simulations have $\beta_{\mathrm{pi}1} = 7$ at single-digit precision, but we still label them as $\beta_{\mathrm{pi}1} \approx 8$ to simplify the presentation. We refer the reader to Table 1 for a complete list of the input parameters of

Table 1
Simulation Input Parameters

Label	$M_{0\mathrm{i}}$	M_s	M_A	β_{pi1}	$T_{\mathrm{e1}}/T_{\mathrm{i1}}$	v_0/c	v_1/c	$\Omega_i t$	x_{shock}	x_{L}	x_{R}	n/n_1	$T_{\mathrm{e2}}/T_{\mathrm{e2,ad}}-1$	$T_{\mathrm{e2}}/T_{\mathrm{e1}}$	$T_{\mathrm{i2}}/T_{\mathrm{i1}}$	$T_{\mathrm{e2}}/T_{\mathrm{i2}}$
M2b1T0.1	2.14	3.45	3.34	1.03	0.10	0.276	0.456	40.66	29.1	−20.0	−10.0	2.45	0.10	1.485	3.282	0.045
M2b1T0.3	2.14	3.24	3.38	1.03	0.32	0.276	0.459	40.66	29.7	−20.0	−10.0	2.42	0.07	1.432	3.213	0.141
M2b1T1.0	2.14	2.79	3.50	1.03	1.00	0.276	0.469	40.66	31.3	−20.0	−10.0	2.34	0.05	1.389	3.076	0.452
M3b1T0.1	3.21	4.41	4.22	1.00	0.10	0.414	0.583	40.13	19.6	−14.0	−6.0	3.13	0.24	1.820	6.429	0.028
M3b1T0.3	3.21	4.12	4.25	1.00	0.32	0.414	0.585	40.13	19.8	−14.0	−6.0	3.09	0.16	1.685	6.349	0.084
M3b1T1.0	3.21	3.53	4.37	1.00	1.00	0.414	0.593	40.13	20.9	−14.0	−6.0	3.02	0.10	1.597	6.094	0.262
M4b1T0.1	4.28	5.32	4.99	0.96	0.10	0.552	0.703	40.17	15.0	−9.0	−4.0	3.85	0.61	2.529	11.369	0.022
M4b1T0.3	4.28	4.96	5.02	0.96	0.32	0.552	0.704	40.17	15.0	−9.0	−4.0	3.85	0.34	2.094	11.174	0.059
M4b1T1.0	4.28	4.21	5.10	0.96	1.00	0.552	0.707	40.17	15.4	−9.0	−4.0	3.83	0.22	1.913	10.773	0.178
M5b1T0.1	5.35	6.15	5.60	0.90	0.10	0.690	0.813	40.32	11.8	−8.0	−2.0	4.73	1.50	4.197	19.901	0.021
M5b1T0.3	5.35	5.74	5.63	0.90	0.32	0.690	0.814	40.32	11.9	−8.0	−2.0	4.72	0.69	2.837	19.827	0.045
M5b1T1.0	5.35	4.85	5.70	0.90	1.00	0.690	0.814	40.32	12.0	−8.0	−2.0	4.70	0.43	2.389	19.323	0.124
M2b2T0.1	2.14	3.32	4.53	2.05	0.10	0.276	0.439	25.16	16.2	−13.0	−8.0	2.59	0.12	1.532	3.531	0.043
M2b2T0.3	2.14	3.12	4.59	2.05	0.32	0.276	0.442	25.16	16.6	−13.0	−8.0	2.55	0.08	1.476	3.446	0.135
M2b2T1.0	2.14	2.68	4.73	2.05	1.00	0.276	0.451	25.16	17.5	−13.0	−8.0	2.46	0.06	1.430	3.286	0.435
M3b2T0.1	3.21	4.31	5.82	2.00	0.10	0.414	0.571	25.99	11.7	−8.0	−3.0	3.24	0.26	1.860	6.796	0.027
M3b2T0.3	3.21	4.04	5.86	2.00	0.32	0.414	0.573	25.99	11.9	−8.0	−3.0	3.23	0.18	1.752	6.687	0.083
M3b2T1.0	3.21	3.45	6.00	2.00	1.00	0.414	0.579	25.99	12.4	−8.0	−3.0	3.13	0.13	1.653	6.455	0.256
M4b2T0.1	4.28	5.24	6.92	1.92	0.10	0.552	0.692	25.62	8.8	−5.0	−2.5	4.07	0.62	2.582	11.875	0.022
M4b2T0.3	4.28	4.88	6.95	1.92	0.32	0.552	0.693	25.62	8.8	−5.0	−2.5	4.02	0.37	2.183	11.766	0.059
M4b2T1.0	4.28	4.15	7.08	1.92	1.00	0.552	0.697	25.62	9.1	−5.0	−2.5	3.94	0.25	1.978	11.401	0.174
M5b2T0.1	5.35	6.08	7.79	1.80	0.10	0.690	0.804	25.45	6.9	−4.0	−1.0	4.97	1.21	3.775	20.591	0.018
M5b2T0.3	5.35	5.67	7.82	1.80	0.32	0.690	0.804	25.45	6.8	−4.0	−1.0	5.00	0.70	2.901	20.264	0.045
M5b2T1.0	5.35	4.79	7.93	1.80	1.00	0.690	0.805	25.45	6.9	−4.0	−1.0	4.97	0.45	2.479	19.676	0.126
M2b4T0.1	2.14	3.24	6.25	4.11	0.10	0.276	0.429	25.77	15.5	−12.0	−5.0	2.67	0.11	1.548	3.755	0.041
M2b4T0.3	2.14	3.05	6.33	4.11	0.32	0.276	0.433	25.77	16.0	−12.0	−5.0	2.62	0.08	1.492	3.648	0.129
M2b4T1.0	2.14	2.62	6.52	4.11	1.00	0.276	0.440	25.77	16.8	−12.0	−5.0	2.53	0.07	1.451	3.430	0.423
M3b4T0.1	3.21	4.21	8.00	4.00	0.10	0.414	0.556	25.15	10.2	−7.0	−2.5	3.55	0.30	1.985	7.045	0.028
M3b4T0.3	3.21	3.94	8.07	4.00	0.32	0.414	0.559	25.15	10.4	−7.0	−2.5	3.46	0.23	1.864	6.863	0.086
M3b4T1.0	3.21	3.36	8.24	4.00	1.00	0.414	0.563	25.15	10.8	−7.0	−2.5	3.42	0.15	1.733	6.520	0.266
M4b4T0.1	4.28	5.16	9.61	3.84	0.10	0.552	0.682	25.99	8.2	−5.5	−1.5	4.34	0.51	2.460	12.202	0.020
M4b4T0.3	4.28	4.81	9.65	3.84	0.32	0.552	0.682	25.99	8.2	−5.5	−1.5	4.35	0.39	2.273	12.088	0.059
M4b4T1.0	4.28	4.07	9.79	3.84	1.00	0.552	0.683	25.99	8.3	−5.5	−1.5	4.30	0.26	2.049	11.456	0.179
M5b4T0.1	5.35	6.02	10.89	3.61	0.10	0.690	0.797	25.20	6.2	−4.0	−1.5	5.36	1.30	4.020	21.084	0.019
M5b4T0.3	5.35	5.62	10.93	3.61	0.32	0.690	0.797	25.20	6.3	−4.0	−1.5	5.33	0.72	3.001	20.813	0.046
M5b4T1.0	5.35	4.76	11.10	3.61	1.00	0.690	0.799	25.20	6.4	−4.0	−1.5	5.25	0.45	2.513	20.440	0.123
M2b8T0.1	2.14	3.17	8.62	8.21	0.10	0.276	0.419	25.16	14.1	−10.0	−5.0	2.81	0.14	1.604	3.977	0.040
M2b8T0.3	2.14	2.98	8.74	8.21	0.32	0.276	0.423	25.16	14.6	−10.0	−5.0	2.76	0.09	1.533	3.854	0.126
M2b8T1.0	2.14	2.56	9.01	8.21	1.00	0.276	0.430	25.16	15.3	−10.0	−5.0	2.65	0.07	1.482	3.587	0.413

Table 1

(Continued)

Label	M_{0i}	M_s	M_A	β_{pi1}	T_{e1}/T_{i1}	v_0/c	v_1/c	$\Omega_i t$	x_{shock}	x_L	x_R	n/n_1	$T_{e2}/T_{e2,ad} - 1$	T_{e2}/T_{e1}	T_{i2}/T_{i1}	T_{e2}/T_{i2}
M3b8T0.1	3.21	4.13	11.08	8.00	0.10	0.414	0.546	25.99	9.7	−7.0	−2.0	3.80	0.29	2.008	7.152	0.028
M3b8T0.3	3.21	3.86	11.16	8.00	0.32	0.414	0.547	25.99	9.8	−7.0	−2.0	3.75	0.22	1.903	6.983	0.086
M3b8T1.0	3.21	3.31	11.48	8.00	1.00	0.414	0.555	25.99	10.5	−7.0	−2.0	3.55	0.14	1.741	6.599	0.264
M4b8T0.1	4.28	5.09	13.40	7.68	0.10	0.552	0.673	25.17	7.3	−5.5	−1.5	4.57	0.62	2.687	12.492	0.022
M4b8T0.3	4.28	4.76	13.50	7.68	0.32	0.552	0.675	25.17	7.5	−5.5	−1.5	4.56	0.38	2.292	12.322	0.059
M4b8T1.0	4.28	4.05	13.75	7.68	1.00	0.552	0.679	25.17	7.7	−5.5	−1.5	4.41	0.24	2.041	11.852	0.172
M5b8T0.1	5.35	6.00	15.30	7.22	0.10	0.690	0.793	25.81	6.1	−5.0	−1.0	5.45	1.42	4.253	21.312	0.020
M5b8T0.3	5.35	5.58	15.35	7.22	0.32	0.690	0.792	25.81	6.1	−5.0	−1.0	5.50	0.77	3.123	21.103	0.047
M5b8T1.0	5.35	4.73	15.57	7.22	1.00	0.690	0.793	25.81	6.2	−5.0	−1.0	5.40	0.51	2.654	20.572	0.129

Note. Columns are defined in Sections 2 and 4 and Appendix C.

(This table is available in machine-readable form.)

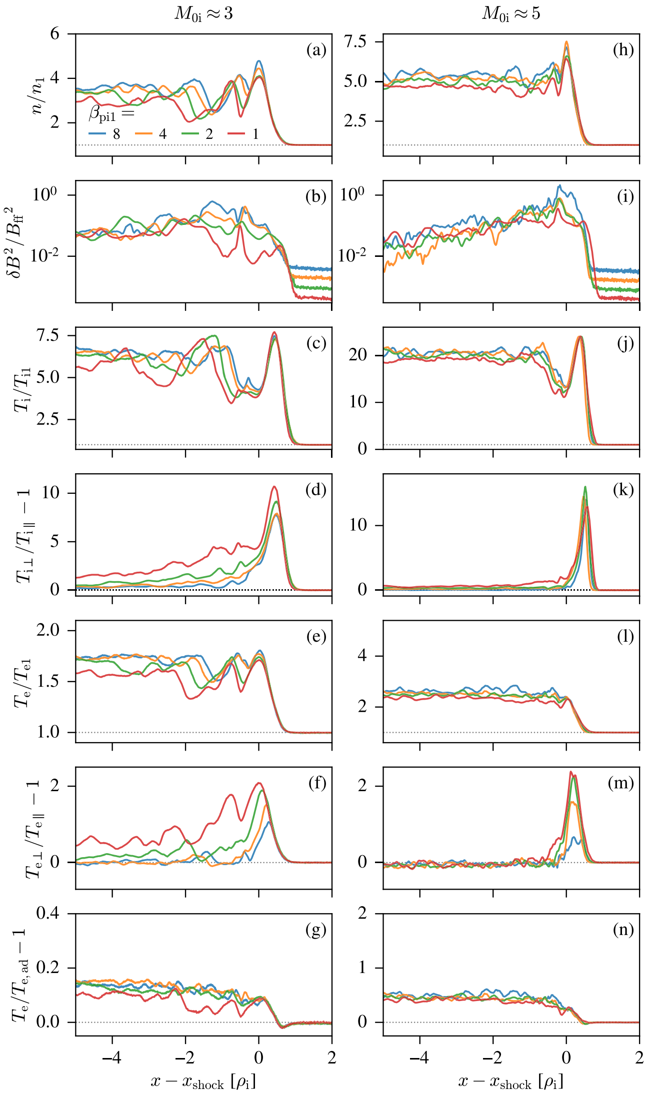

Figure 1. Dependence on M_{0i} and β_{pi1} of various y-averaged quantities measured at $\Omega_i t \sim 25$ (with the exception of $\beta_{pi1} = 1$, which is measured at $\Omega_i t \sim 40$), for a preshock temperature ratio $T_{e1}/T_{i1} = 1$ (runs `M3b1T1.0` − `M3b8T1.0` in the left column; runs `M5b1T1.0` − `M5b8T1.0` in the right column). The x coordinate is measured relative to the shock location in units of the proton Larmor radius ρ_i. From top to bottom, we plot: (a) rest-frame number density; (b) energy in magnetic fluctuations, normalized to the energy of the frozen-in field (see text); (c) mean proton temperature (see text); (d) proton temperature anisotropy; (e) mean electron temperature; (f) electron temperature anisotropy; (g) excess of electron temperature beyond the adiabatic prediction for an isotropic 3D ultrarelativistic gas. Note that the vertical axis range is different between the left and right columns.

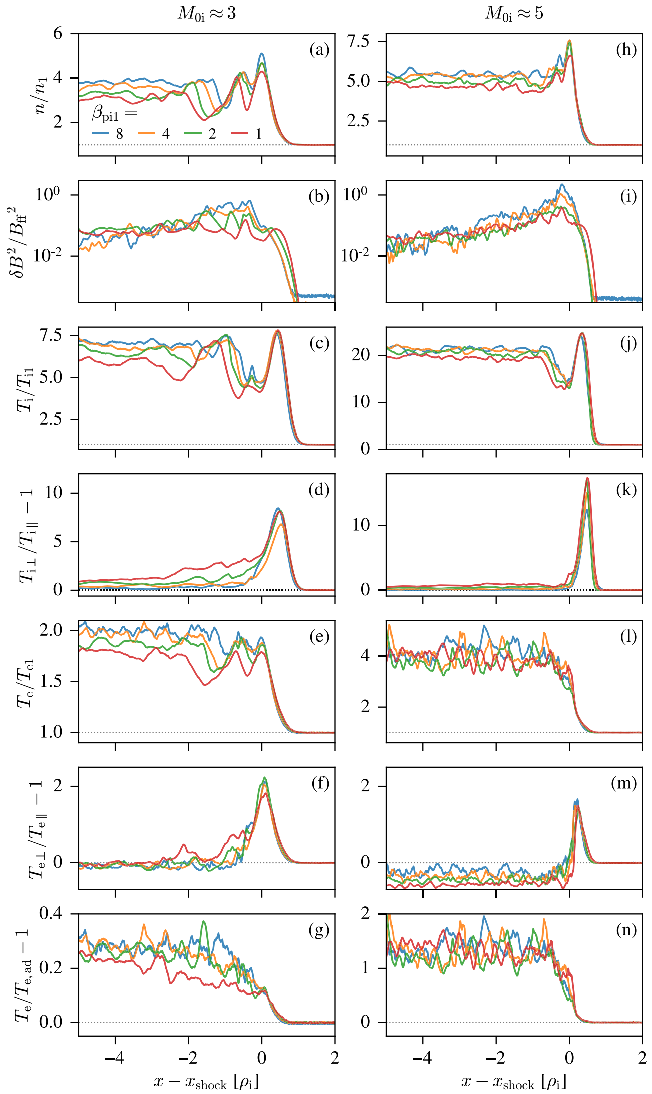

Figure 2. Like Figure 1, but for $T_{e1}/T_{i1} = 0.1$ (runs `M3b1T0.1` − `M3b8T0.1` in the left column; runs `M5b1T0.1` − `M5b8T0.1` in the right column).

our simulations and the convention used to identify our runs (e.g., run `M2b1T0.1` has $M_{0i} \approx 2$, $\beta_{pi1} \approx 1$, and $T_{e1}/T_{i1} = 0.1$).

3. Shock Structure

The dependence of the shock structure on the upstream conditions is illustrated in Figures 1–4. Figures 1 and 2 show y-averaged quantities as a function of the Mach number (in each figure, $M_{0i} \approx 3$ in the left column and $M_{0i} \approx 5$ in the right column), the ion plasma beta (different colors in each plot; see legend in panel (a)), and the electron-to-ion temperature ratio ($T_{e1}/T_{i1} = 1$ in Figure 1 and $T_{e1}/T_{i1} = 0.1$ in Figure 2). We first discuss the dependence on the Mach number and the ion plasma beta, and then on the electron-to-proton temperature ratio.

In agreement with the Rankine–Hugoniot relations, the ion density jump is larger for higher M_{0i} (compare panels (a) and (h) in Figures 1 and 2); we take $n = n_i$, with $n_i \approx n_e$ within a few percent. In regards to the dependence on β_{pi1}, it is rather modest, with only marginal evidence for weaker compressions in the most magnetized case of $\beta_{pi1} = 1$. As a result of flux freezing alone, one would expect the lab-frame magnetic field to be $B_{\rm ff} = (\langle n \rangle_y / n_0) B_0$, where $\langle \cdot \rangle_y$ denotes averaging along the y-direction. In reality, the magnetic field energy at the shock and in the downstream region exceeds the expectation from flux freezing due to self-generated magnetic fluctuations. Their strength is quantified by $\delta B^2 = B_x^2 + (B_y - B_{\rm ff})^2 + B_z^2$ in panels (b) and (i) of Figures 1 and 2. As we further discuss below, the relaxation of ion velocity–space anisotropies can result in proton cyclotron modes and mirror modes (for a review of anisotropy instabilities in relativistic plasmas, see Galishnikova et al. 2023). For the magnetic geometry employed in this paper, proton cyclotron waves would appear in B_x and B_z, and their wavevector is aligned with the mean field; in contrast, mirror modes appear in B_x and B_y, and their

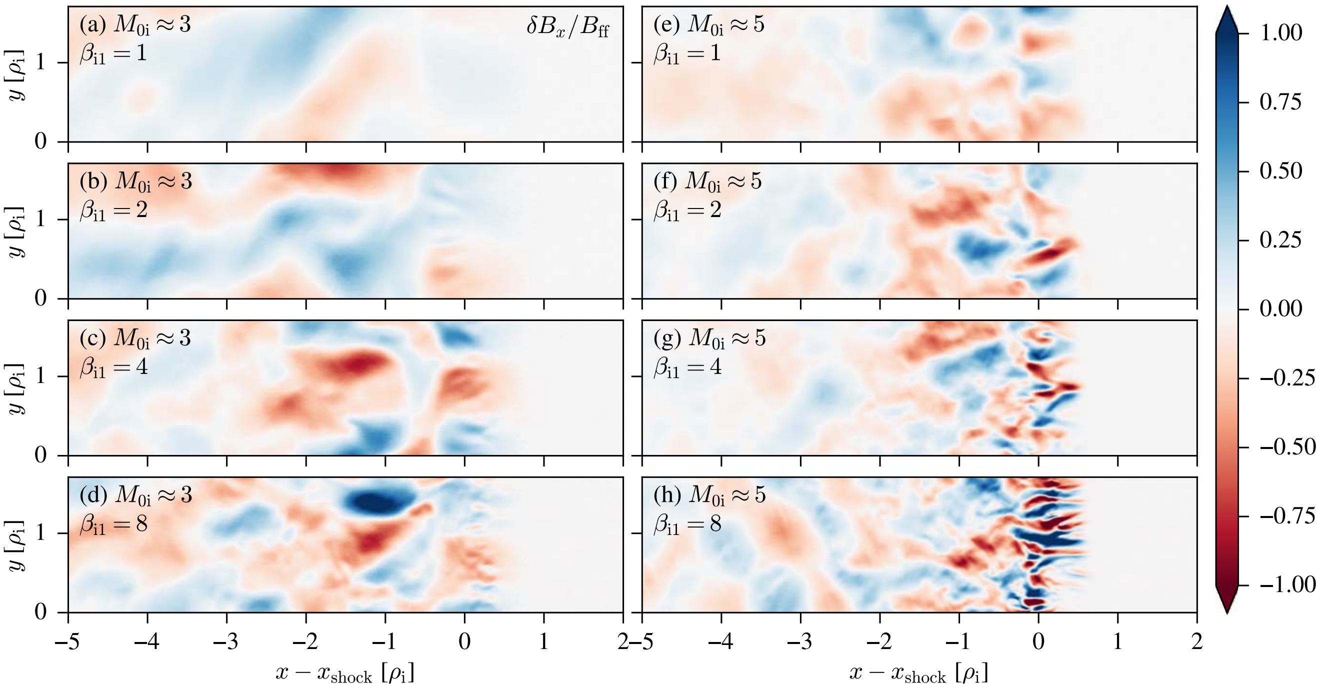

Figure 3. Dependence on M_{0i} and β_{pi1} of the fluctuating magnetic field component $\delta B_x/B_{ff}$ measured at $\Omega_i t \sim 25$ (for $\beta_{pi1} = 1$, $\Omega_i t \sim 40$), assuming $T_{e1}/T_{i1} = 1$ (runs `M3b1T1.0` – `M3b8T1.0` in the left column; runs `M5b1T1.0` – `M5b8T1.0` in the right column). The field is measured in the simulation frame, and the x coordinate is measured relative to the shock location.

wavevector is oblique with respect to the mean field. In Figures 3 and 4, we show the x component $\delta B_x/B_{ff} = B_x/B_{ff}$, which includes both proton cyclotron and mirror modes. We find that proton cyclotron modes dominate near the shock.

We define the isotropic-equivalent proton temperature $T_i = (2T_{i\perp} + T_{i\|})/3$, which we present in panels (c) and (j) of Figures 1 and 2. We define $T_{i\perp}$ as the proton temperature perpendicular to the mean field, and $T_{i\|}$ as the proton temperature along the mean field. Both $T_{i\perp}$ and $T_{i\|}$ are computed in the proton fluid's local rest frame; likewise, electron temperatures $T_{e\perp}$ and $T_{e\|}$ are computed in the electron fluid's local rest frame. It is apparent that T_i/T_{i1} increases with M_{0i}, which comes from the fact that the temperature jump predicted by the Rankine–Hugoniot relations for the overall fluid is a monotonic function of $M_s \sim M_{0i}$, and that most of the postshock fluid energy resides in protons (rather than electrons or proton-driven waves).

At the shock, magnetic fluctuations are sourced by the relaxation of the proton temperature anisotropy $T_{i\perp}/T_{i\|}$ (panels (d) and (k) in Figures 1 and 2), which is larger for higher M_{0i}. This has two consequences: (i) the greater amount of free energy stored in proton temperature anisotropy for higher M_{0i} generates stronger waves (compare panels (b) and (i) in Figures 1–2); (ii) linear theory prescribes that the waves grow faster for higher levels of anisotropy (so, higher M_{0i}). In fact, panels (b) and (i) in Figures 1 and 2 show that the peak of wave activity is located right at the shock for $M_{0i} \approx 5$, but shifts farther downstream for lower M_{0i}, due to the slower wave growth. Regarding the dependence on β_{pi1}, we find that the proton anisotropy at the shock is nearly insensitive to β_{pi1}. However, proton-generated waves are stronger for higher β_{pi1}, when normalized to the flux-frozen field (see panels (b) and (i) in Figures 1–2, as well as Figures 3 and 4). This is because the free energy in proton anisotropy available to source the waves is larger for higher β_{pi1}, when compared to the magnetic energy of the background field.

Due to pitch angle scattering by the proton modes, the proton anisotropy drops behind the shock at a faster rate for higher M_{0i} and higher β_{pi1}, since the waves grow faster and are stronger. Far downstream, the proton anisotropy is expected to be reduced below a marginal stability threshold, which is lower at higher plasma beta for both mirror and proton cyclotron modes. A decrease in anisotropy with increasing β_{pi1} is apparent in panels (d) and (k) of Figures 1 and 2, especially at low M_{0i}. It is worth noting that low-β_{pi1} low-M_{0i} shocks maintain an appreciable degree of proton anisotropy in the far downstream, so the resulting adiabatic index will be larger than for a 3D isotropic gas. Then the plasma will be less compressible, which explains why the red curve in the density profile of panels (a) and (h) lies below the other lines.

So far, we have focused on the proton physics. In regards to electrons, we find that the isotropic-equivalent postshock electron temperature $T_e = (2T_{e\perp} + T_{e\|})/3$ increases for greater M_{0i} (compare panels (e) and (l) in Figures 1 and 2). This might just follow from the dependence on M_{0i} of the adiabatic heating efficiency, since the density compression increases with M_{0i}. However, the efficiency of irreversible electron heating is also higher at larger M_{0i}. In panels (g) and (n), we present the excess of electron temperature beyond the adiabatic expectation $T_{e,ad} = (n/n_1)^{1/3} T_{e1}$ appropriate for a 3D isotropic ultrarelativistic gas. The assumption of isotropic electrons is well justified in the downstream region, where $T_{e\perp} \simeq T_{e\|}$ (panels (f) and (m) in Figures 1 and 2).

A large fraction of the electron irreversible heating comes from magnetic pumping (Berger et al. 1958; Hollweg 1985; Borovsky 1986; Guo et al. 2017; Ley et al. 2023). In this mechanism, two ingredients are needed: (i) the presence of an electron temperature anisotropy, which in our case is induced by field amplification coupled to adiabatic invariance, and (ii) a

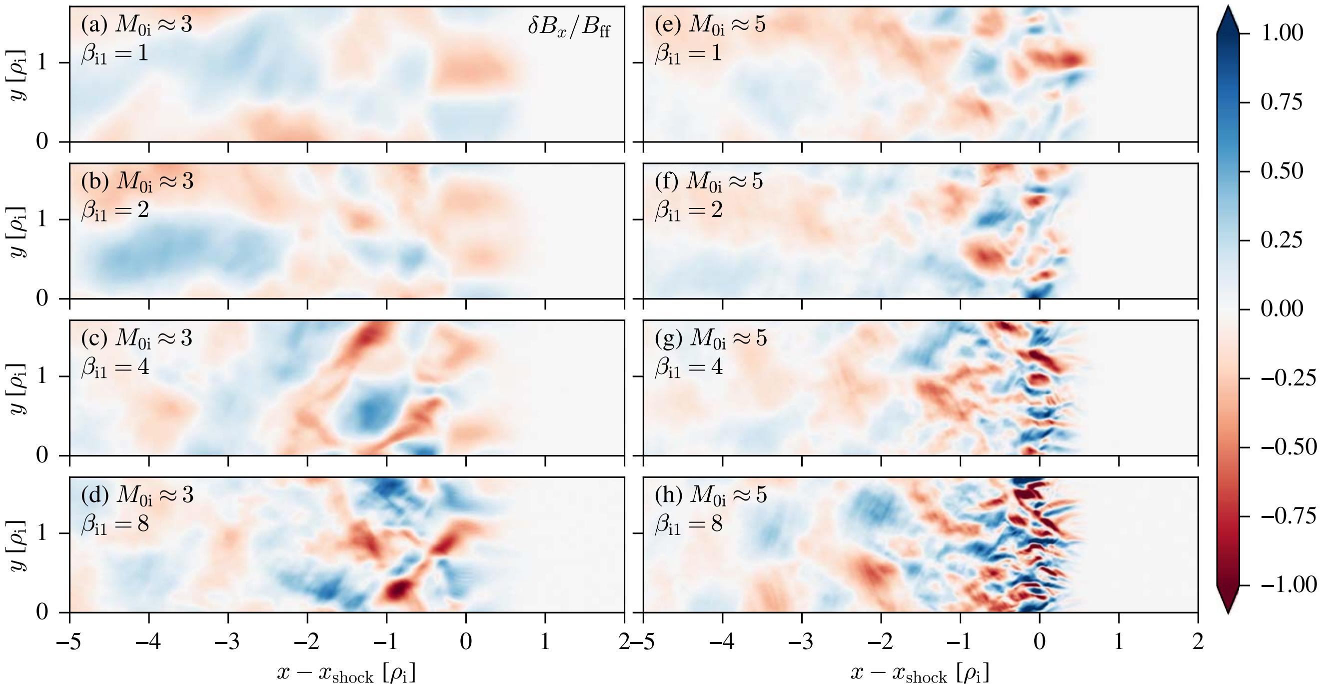

Figure 4. Like Figure 3, but for $T_{e1}/T_{i1} = 0.1$ (runs `M3b1T0.1 − M3b8T0.1` on the left; runs `M5b1T0.1 − M5b8T0.1` on the right).

mechanism to break the electron adiabatic invariance. Field amplification in our shocks has two potential drivers: at the shock ramp, density compression coupled to flux freezing leads to field amplification; in addition, at the shock front and further downstream, proton waves accompanying the relaxation of the proton temperature anisotropy contribute to further field growth. Regarding the mechanism for breaking the electron adiabatic invariance, in nonrelativistic low-M_s and high-β_{pi1} shocks it was attributed to pitch angle scattering by whistler waves sourced by the electron anisotropy itself (Guo et al. 2017, 2018; Ha et al. 2021; Kim et al. 2021; Ley et al. 2024). For the transrelativistic conditions of this work ($\theta_i \lesssim 1$ and $\theta_e \gg 1$), the ratio between proton and electron Larmor radii (which roughly corresponds to the ratio of proton cyclotron wavelength to whistler wavelength) is $\sim(T_i/T_e)/\sqrt{\theta_i}$. At the shock $\theta_i \sim 0.1$ and T_i/T_e is a few times larger than T_{i1}/T_{e1} (see Figures 1 and 2). This implies that the proton cyclotron wavelength is larger than the whistler wavelength, but their ratio is smaller than for nonrelativistic temperatures, where it is $\sim\sqrt{m_i T_i/(m_e T_e)} \gg 1$. The presence of short-wavelength electron whistler waves is mostly supported by the $M_{0i} \approx 3$ cases (Figures 3(b)–(d) and 4(d)). For $M_{0i} \approx 5$, proton-driven modes grow quickly and reach strong amplitudes. They dominate the wave energy at the shock, hiding the potential presence of whistler waves.

The amount of superadiabatic electron heating is nearly independent of β_{pi1}, with the exception of $\beta_{pi1} = 1$ in the $M_{0i} \approx 3$ shock (red line in panel (g) of Figures 1 and 2). This case displays the lowest density compression and the weakest level of proton-driven waves (see panel (b) in the same figures), so it lacks a sufficient degree of field amplification to drive efficient superadiabatic electron heating via the pumping mechanism. In contrast, electron heating beyond the adiabatic expectation is a strong function of M_{0i}. First of all, the electron fluid suffers a stronger compression while passing through the ramp of a higher-M_{0i} shock (Guo et al. 2017, 2018). In addition, the highly anisotropic protons present in higher-M_{0i} shocks generate stronger proton modes. In both cases, stronger field amplification at higher-M_{0i} shocks performs more work on the electrons and ultimately leads to greater electron heating.

By comparing Figures 1 and 2 (panels (g) and (n)), we infer that the amount of superadiabatic heating is larger for $T_{e1}/T_{i1} = 0.1$ than for $T_{e1}/T_{i1} = 1$, by roughly a factor of 2. As we further discuss in Section 4, this trend cannot be explained by the magnetic pumping framework discussed so far. In fact, both the amount of field amplification (panels (b) and (i)) as well as the degree of electron anisotropy (panels (f) and (m)) are nearly insensitive to T_{e1}/T_{i1}, at fixed β_{pi1} and M_{0i}. Thus, we would expect comparable amounts of pumping-driven heating for $T_{e1}/T_{i1} = 0.1$ and $T_{e1}/T_{i1} = 1$ (we will confirm in Section 4 that this is indeed the case). Below, we demonstrate that the greater heating efficiency of $T_{e1}/T_{i1} = 0.1$ shocks is due to the dominant contribution of B-parallel electric fields (i.e., $E_\parallel = \boldsymbol{E} \cdot \boldsymbol{B}/B$). Heating by $E_\parallel$ tends to increase $T_{e\parallel}$, which explains why $T_{e\perp} < T_{e\parallel}$ in panel (m) of Figure 2.

4. Electron Heating Efficiency and Mechanism

We now characterize the efficiency of electron heating in our shocks as a function of the proper sonic Mach number M_s. We measure the particle density n_2 and the isotropic-equivalent temperatures T_{e2} and T_{i2} in a region that is sufficiently far downstream that the temperatures have reached a quasi-steady value (see Appendix B and Table 1 for details on the region chosen to compute the downstream values of density and temperature). The postshock electron temperature exceeds the adiabatic expectation $T_{e2,ad} = (n_2/n_1)^{1/3} T_{e1}$ by the amount indicated in Figure 5(a). There, different colors indicate different β_{pi1} (see the legend), while different symbols specify the value of T_{e1}/T_{i1}: triangles for $T_{e1}/T_{i1} = 1$, diamonds for $T_{e1}/T_{i1} = 0.3$, circles for $T_{e1}/T_{i1} = 0.1$. The amount of superadiabatic heating is nearly independent from β_{pi1} and T_{e1}/T_{i1}, and it is an increasing function of M_s. Its dependence on M_s can

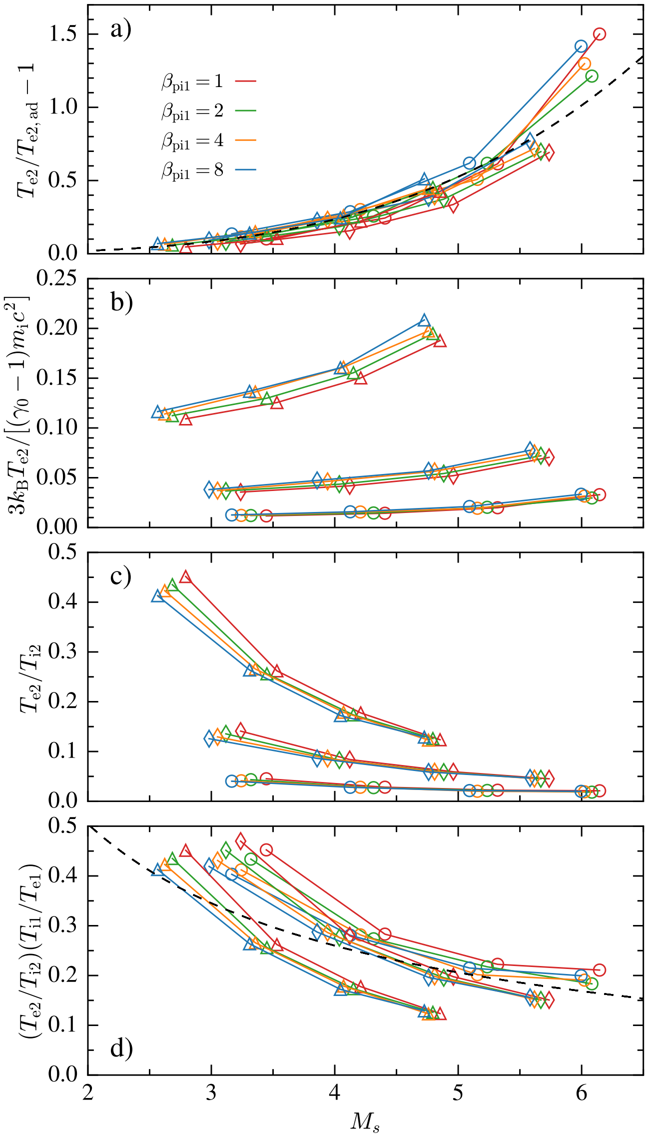

Figure 5. Amount of superadiabatic electron heating (panel (a)), downstream electron thermal energy normalized to upstream flow energy measured in downstream frame (panel (b)), and postshock electron-to-ion temperature ratio (panels (c) and (d)), all as a function of M_s (horizontal axis), $\beta_{\rm pi1}$ (colors, see legend) and $T_{\rm e1}/T_{\rm i1}$ (triangles for $T_{\rm e1}/T_{\rm i1} = 1$, diamonds for $T_{\rm e1}/T_{\rm i1} = 0.3$, circles for $T_{\rm e1}/T_{\rm i1} = 0.1$). Panels (a), (b), and (c) present our raw data, while panel (d) condenses the dependence on preshock parameters in a simpler form.

be parameterized as

$$T_{\rm e2}/T_{\rm e2,ad} - 1 \simeq 0.0016 M_s^{3.6} \tag{1}$$

as indicated by the dashed line. In Figure 5(b) we show the electron thermal energy $3k_{\rm B}T_{\rm e2}$, comprising both adiabatic and superadiabatic heating, normalized to the bulk upstream flow kinetic energy $(\gamma_0 - 1)m_{\rm i}c^2$ measured in the downstream rest frame.

We also present the dependence on $\beta_{\rm pi1}$, M_s, and $T_{\rm e1}/T_{\rm i1}$ of the postshock electron-to-ion temperature ratio $T_{\rm e2}/T_{\rm i2}$ in Figure 5(c). The dependence on $\beta_{\rm pi1}$ is weak, while the dependence on M_s and $T_{\rm e1}/T_{\rm i1}$ can be approximately cast as $(T_{\rm e2}/T_{\rm i2})(T_{\rm i1}/T_{\rm e1}) \simeq M_s^{-0.8} - 0.07$ (dashed line in Figure 5(d)). In all cases $T_{\rm e2}/T_{\rm i2} < T_{\rm e1}/T_{\rm i1}$, i.e., shocks systematically lead to temperature disequilibration.

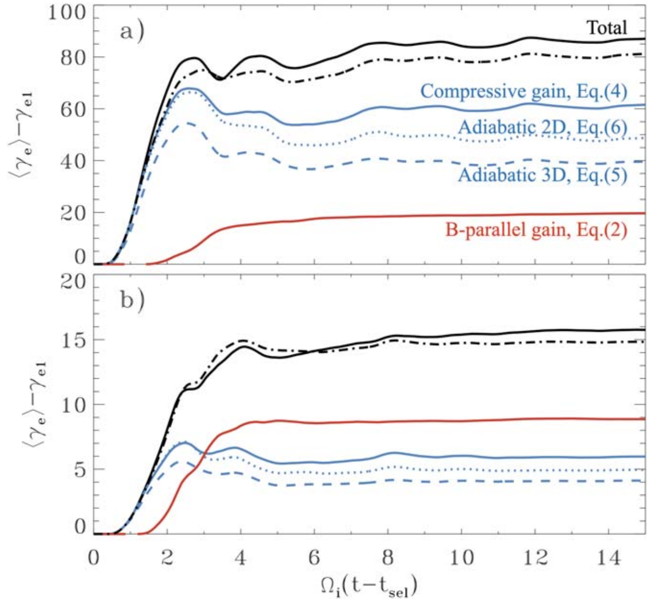

Figure 6. Time evolution of the mean energy of a population of electrons tracked during their passage through the shock, as measured in the local $E \times B$ frame. We fix $M_{0\rm i} \approx 5$ and $\beta_{\rm pi1} \approx 2$ and explore two cases: $T_{\rm e1}/T_{\rm i1} = 1$ at the top (run `M5b2T1.0`) and $T_{\rm e1}/T_{\rm i1} = 0.1$ at the bottom (run `M5b2T0.1`). As described in the legend, the black solid line indicates $\langle\gamma_{\rm e}\rangle - \gamma_{\rm e1}$; the red line illustrates the work done by B-parallel electric fields; the blue solid line indicates heating by magnetic compression, while the dashed and dotted blue lines correspond to the adiabatic expectations for a 3D and 2D gas, respectively (see text for details); superadiabatic heating via magnetic pumping is the difference between solid and dashed blue lines; the dotted–dashed black line is the sum of the red and blue solid lines.

In Figures 6 and 7, we consider shocks with $M_{0\rm i} = 5$ and investigate the dominant mechanisms of electron heating. In Figure 6, we also fix $\beta_{\rm pi1} = 2$ and compare two cases: $T_{\rm e1}/T_{\rm i1} = 1$ (top) and $T_{\rm e1}/T_{\rm i1} = 0.1$ (bottom). At time $t_{\rm sel}$ (where $\Omega_{\rm i} t_{\rm sel} \sim 40$ for $\beta_{\rm pi1} = 1$ and $\Omega_{\rm i} t_{\rm sel} \sim 25$ for all other cases), we select a slab of electrons just upstream of the shock foot, having roughly the same initial x location (within 10%). Each simulation selects approximately 0.5 million electrons. We follow them in time until they propagate far enough behind the shock that their mean energy approaches roughly a constant value. Their properties are recorded with an output cadence of 50 time steps $= 7.5/\omega_{\rm pe}$. In Figure 6, we define $\gamma_{\rm e1} \simeq 3\,\theta_{\rm e1}$ as their initial mean Lorentz factor in the electron rest frame, while $\langle\gamma_{\rm e}\rangle$ (black solid lines in Figure 6) is obtained, at any subsequent time, as an average over the electron population. At every time, we boost each electron to the frame that moves with the local $\boldsymbol{v}_{E\times B} = c(\boldsymbol{E} \times \boldsymbol{B})/B^2$ (hereafter, the $E \times B$ frame). In this frame, we compute the Lorentz factor $\gamma_{\rm e}$ of each electron and the population-averaged value $\langle\gamma_{\rm e}\rangle$. Since electrons in our runs are always ultrarelativistic, the mean Lorentz factor $\langle\gamma_{\rm e}\rangle \simeq 3\theta_{\rm e}$ is always a good proxy for the electron thermal energy.

In the $E \times B$ frame, we also measure the work done by B-parallel electric fields (red lines in Figure 6) as

$$(\langle\gamma_{{\rm e},E_\parallel}\rangle - \gamma_{\rm e1}) m_{\rm e} c^2 = \left\langle \int -eE_\parallel v_\parallel dt \right\rangle \tag{2}$$

where $\langle\cdot\rangle$ stands for an average over the electrons we are tracking, and $v_\parallel$ is the B-parallel 3-velocity of an individual electron in the local $E \times B$ frame, where $E_\parallel$ is also computed. The work done by magnetic field compression, assuming

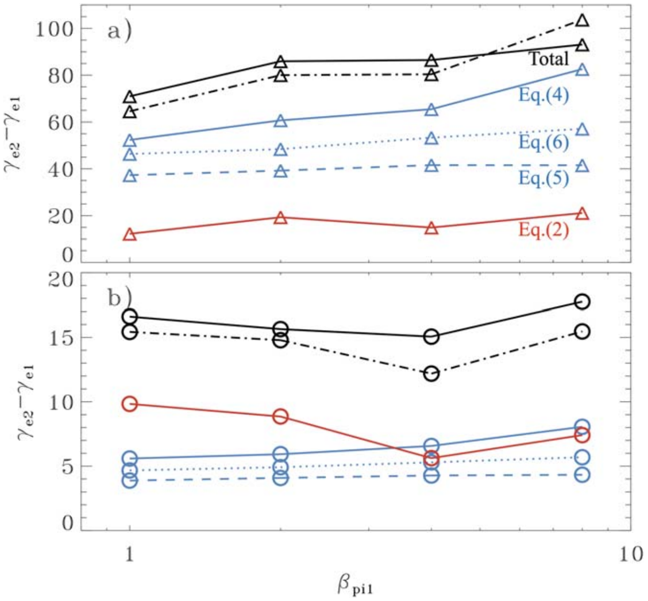

Figure 7. Contributions of various heating mechanisms to the mean energy change of the tracked electrons, as measured in the local $E \times B$ frame. We fix $M_{0\rm i} \approx 5$ and explore the dependence on $\beta_{\rm pi1}$ (horizontal axis) and $T_{\rm e1}/T_{\rm i1}$ ($T_{\rm e1}/T_{\rm i1} = 1$ at the top and $T_{\rm e1}/T_{\rm i1} = 0.1$ at the bottom). Thus, we employ runs `M5b1T1.0` – `M5b8T1.0` at the top and runs `M5b1T0.1` – `M5b8T0.1` at the bottom. The data points are obtained by time-averaging the heating curves (e.g., the ones in Figure 6) at $\Omega_{\rm i}(t - t_{\rm sel}) \gtrsim 8$. The color coding and the line style correspond to Figure 6 (see also the legend): the black points indicate $\gamma_{\rm e2} - \gamma_{\rm e1}$; the red points illustrate the work done by B-parallel electric fields; the blue points connected by solid lines indicate heating by magnetic compression, while the dashed and dotted blue lines correspond to the adiabatic expectations for a 3D and 2D gas, respectively; superadiabatic heating via magnetic pumping is the difference between solid and dashed blue lines; the black points connected by dotted–dashed black lines are the sum of magnetic compression and B-parallel heating.

conservation of the adiabatic invariants $\gamma\beta_{\|}$ and $(\gamma\beta_{\perp})^2/B$, can be computed as follows. First, the change in Lorentz factor for each electron between time step n and $n+1$ is calculated as in Tran & Sironi (2020),

$$\gamma_{n\to n+1,\rm B} = \sqrt{1 + (\gamma\beta_{\|})_n^2 + (\gamma\beta_{\perp})_n^2\,(B_{n+1}/B_n)} \tag{3}$$

where $\beta_{\|} = v_{\|}/c$, while $\beta_{\perp}$ is the dimensionless electron velocity perpendicular to the local magnetic field, both measured in the $E \times B$ frame. The electron Lorentz factor in the $E \times B$ frame is $\gamma = 1\Big/\sqrt{1 - \beta_{\|}^2 - \beta_{\perp}^2}$. When averaged over the population of tracked electrons (blue solid lines in Figure 6), we have

$$\langle\gamma_{\rm e,B}\rangle - \gamma_{\rm e1} = \langle\Sigma_n(\gamma_{n\to n+1,\rm B} - \gamma_n)\rangle\ . \tag{4}$$

The compressive contribution $\langle\gamma_{\rm e,B}\rangle$ can be compared with the adiabatic expectation for a 3D isotropic ultrarelativistic gas (dashed blue lines in Figure 6)

$$\langle\gamma_{\rm e,ad3D}\rangle = \langle(n/n_1)^{1/3}\gamma_1\rangle \tag{5}$$

(where the density n is measured in the local $E \times B$ frame, and γ_1 is the preshock Lorentz factor of an individual electron, such that $\gamma_{\rm e1} = \langle\gamma_1\rangle$), or with the expectation for a 2D fluid that preserves the adiabatic invariants since the beginning (dotted blue lines in Figure 6)

$$\langle\gamma_{\rm e,ad2D}\rangle = \langle\sqrt{1 + (\gamma\beta_{\|})_1^2 + (\gamma\beta_{\perp})_1^2\,(B/B_1)}\rangle \tag{6}$$

where the subscript 1 indicates initial conditions of each electron (i.e., at the selection time $t_{\rm sel}$). In the absence of pitch angle scattering, the adiabatic invariants would be preserved, and the electron mean Lorentz factor would evolve as $\langle\gamma_{\rm e}\rangle = \langle\gamma_{\rm e,B}\rangle = \langle\gamma_{\rm e,ad2D}\rangle$.

We remark that superadiabatic heating via magnetic pumping is quantified by the difference $\langle\gamma_{\rm e,B}\rangle - \langle\gamma_{\rm e,ad3D}\rangle$ (i.e., the difference between solid and dashed blue lines in Figure 6). Also, the overall amount of superadiabatic heating $T_{\rm e2} - T_{\rm e2,ad}$ discussed before is proportional to the difference between the black solid line and blue dashed line at late times (in the ultrarelativistic limit, $\theta_{\rm e} = \gamma_{\rm e}/3$).

In Figure 6, the dotted–dashed black lines illustrate the combined contributions of B-parallel heating and magnetic compression, showing that their sum is a good proxy for the overall heating curve (black solid lines), for both $T_{\rm e1}/T_{\rm i1} = 1$ (top) and $T_{\rm e1}/T_{\rm i1} = 0.1$ (bottom). We now comment on the trends established after the heating curves have reached a nearly constant value, i.e., $\Omega_{\rm i}(t - t_{\rm sel}) \gtrsim 8$. Standard adiabatic compression ($\langle\gamma_{\rm e,ad3D}\rangle$, dashed blue lines) accounts for ~50% of the overall heating at $T_{\rm e1}/T_{\rm i1} = 1$ and for ~25% at $T_{\rm e1}/T_{\rm i1} = 0.1$. For both $T_{\rm e1}/T_{\rm i1} = 1$ and $T_{\rm e1}/T_{\rm i1} = 0.1$, irreversible heating by magnetic pumping (i.e., the difference between solid and dashed blue lines) amounts to ~50% of the 3D adiabatic expectation. Heating by B-parallel electric fields contributes ~25% of the overall heating at $T_{\rm e1}/T_{\rm i1} = 1$ and ~50% at $T_{\rm e1}/T_{\rm i1} = 0.1$.

At $\Omega_{\rm i}(t - t_{\rm sel}) \gtrsim 8$, heating by magnetic compression (solid blue lines) scales such that $\langle\gamma_{\rm e,B}\rangle/\gamma_{\rm e1} - 1$ is roughly independent of $T_{\rm e1}/T_{\rm i1}$. It follows that the main reason why the overall $\langle\gamma_{\rm e}\rangle/\gamma_{\rm e1} - 1$ is larger for $T_{\rm e1}/T_{\rm i1} = 0.1$ than for $T_{\rm e1}/T_{\rm i1} = 1$ (see also Figure 5(a)) is the additional contribution of B-parallel electric field work.

The same conclusions can be extracted from Figure 7, where we present the contributions of various heating mechanisms to the far-downstream electron mean energy, as a function of $\beta_{\rm pi1}$ and $T_{\rm e1}/T_{\rm i1}$. We find that, in most cases, the sum of B-parallel heating and magnetic compression can account for the overall electron energy change. Regarding superadiabatic heating, magnetic pumping dominates for higher $T_{\rm e1}/T_{\rm i1}$ and, at fixed $T_{\rm e1}/T_{\rm i1}$, it increases with $\beta_{\rm pi1}$ (it amounts to a fraction ~50% of the 3D adiabatic expectation at $\beta_{\rm pi1} = 1$ and ~100% at $\beta_{\rm pi1} = 8$). In contrast, irreversible heating by B-parallel electric fields dominates for $T_{\rm e1}/T_{\rm i1} = 0.1$. As we have already remarked, heating by magnetic compression scales such that $\langle\gamma_{\rm e,B}\rangle - \gamma_{\rm e1} \propto \gamma_{\rm e1}$, at each fixed $\beta_{\rm pi1}$. In contrast, the contribution $\langle\gamma_{\rm e,E_{\|}}\rangle - \gamma_{\rm e1}$ by B-parallel electric field work has a shallower scaling, since it increases by less than a factor of 3 between $T_{\rm e1}/T_{\rm i1} = 0.1$ and $T_{\rm e1}/T_{\rm i1} = 1$.

5. Discussion and Conclusions

In this paper, we have used 2D PIC simulations to quantify the efficiency and mechanisms of electron heating at the collisionless shocks detected in GRMHD simulations of tilted accretion disks. For geometrically thick, radiatively inefficient accretion flows, these shocks have transrelativistic speed, moderate plasma beta, and low sonic Mach number—a parameter regime still largely unexplored. We find that the postshock electron temperature $T_{\rm e2}$

exceeds the adiabatic expectation $T_{\mathrm{e2,ad}}$ by approximately $T_{\mathrm{e2}}/T_{\mathrm{e2,ad}} - 1 \simeq 0.0016 M_s^{3.6}$, nearly independent of the plasma beta and of the temperature ratio. This approximation may be used to incorporate the efficiency of shock-driven electron heating into GRMHD simulations of tilted accretion disks. We also investigate the mechanisms of electron heating and find that for $M_{0\mathrm{i}} = 5$ (i.e., $M_s \sim 5$–6) it is governed by magnetic pumping at $T_{\mathrm{e1}}/T_{\mathrm{i1}} = 1$, while heating by B-parallel electric fields dominates at $T_{\mathrm{e1}}/T_{\mathrm{i1}} = 0.1$.

Our results have been obtained for strictly perpendicular shocks. We expect that our conclusions will also apply to quasi-perpendicular superluminal shocks (see Appendix A for a discussion of the boundary between subluminal and superluminal configurations), while different outcomes may be expected for quasi-perpendicular subluminal shocks, where shock-reflected electrons can propagate back upstream (for a study of electron heating in nonrelativistic quasi-perpendicular shocks, see Tran & Sironi 2024). In quasi-parallel shocks, protons can be efficiently reflected back upstream and accelerated via the Fermi process, and the electron heating physics is likely to be strongly affected by the properties of nonthermal protons and their self-generated waves. Such an investigation will be the subject of future work.

Acknowledgments

Conversations with Jordy Davelaar, Jason Dexter, Charles Gammie, Francisco Ley, Matthew Liska, Nick Kaaz, Eliot Quataert, Chris White, and Ellen Zweibel are gratefully acknowledged. We thank the referee for their constructive comments. A.T. and L.S. were partly supported by NASA ATP 80NSSC20K0565. A.T. was partly supported by NASA FINESST 80NSSC21K1383 and NSF PHY-2010189. L.S. acknowledges support from DoE Early Career Award DE-SC0023015. This work was supported by a grant from the Simons Foundation (MP-SCMPS-00001470) to L.S. and facilitated by Multimessenger Plasma Physics Center (MPPC), NSF grant PHY-2206609. This work was expedited by NASA's Astrophysics Data System, Jonathan Sick's and Rui Xue's `ads2bibdesk`, Benty Fields, and the Python / Matplotlib / Numpy stack. L.S. is grateful for the hospitality of the KITP, which is funded by NSF PHY-1748958.

Appendix A
Superluminal and Subluminal Shock Regimes

Our simulation results are obtained for perpendicular shocks, but we expect they should also apply to oblique superluminal shocks with $\theta'_{Bn1} \gtrsim 70°$, where θ'_{Bn1} is the angle between the upstream magnetic field and shock normal as measured in the shock frame. Figure 8 shows the super/subluminal boundary $v_1 \tan\theta'_{Bn1} = c$ (Drury 1983; Kirk & Heavens 1989; Begelman & Kirk 1990) as a function of M_s and θ'_{Bn1} for the specific transrelativistic shock parameters ($m_{\mathrm{i}}/m_{\mathrm{e}}$, θ_{i1}, $T_{\mathrm{e1}}/T_{\mathrm{i1}}$) used in this manuscript.[4] The upstream sound speed c_{s1} is defined as in Section 2. Transrelativistic superluminal shocks span a wide θ'_{Bn1} interval; in contrast, nonrelativistic shocks with $v_1 \ll c$ and $M_s \sim 1$–10 are superluminal only for θ'_{Bn1} much closer to 90°, see Tran & Sironi (2024).

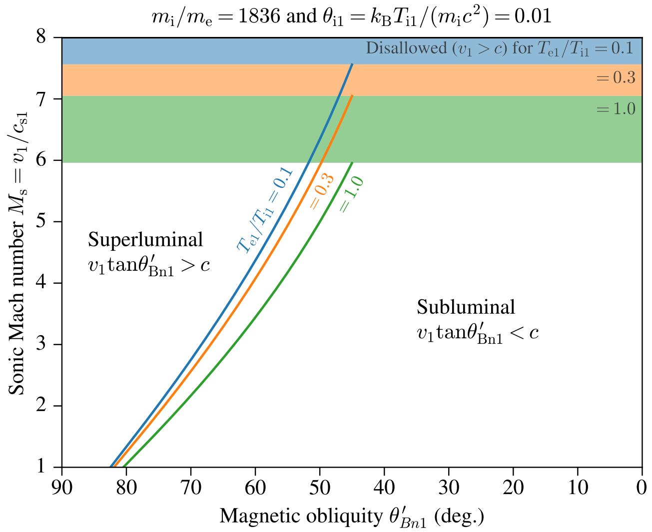

Figure 8. Regime map of superluminal vs. subluminal shocks in (M_s, θ'_{Bn1}) parameter space for varying $T_{\mathrm{e1}}/T_{\mathrm{i1}} = 0.1$ (blue), 0.3 (orange), and 1.0 (green). Here, θ'_{Bn1} is the angle between the upstream magnetic field and the shock normal as measured in the shock frame. Shocks transition from sub- to superluminal as θ'_{Bn1} approaches 90°; the range of superluminal θ'_{Bn1} expands as M_s increases. Because v_1 cannot exceed c, the Mach number $M_s = v_1/c_{s1}$ cannot exceed ∼6–8; the upper bounds on M_s for each $T_{\mathrm{e1}}/T_{\mathrm{i1}}$ are shown by the shaded horizontal bars.

Appendix B
Electron Heating Measurement Regions

Figures 9 and 10 show, for two example shocks, the spatial region $x - x_{\mathrm{shock}} \in [x_{\mathrm{L}}, x_{\mathrm{R}}]$ wherein we measure the isotropic-equivalent temperatures T_{e2} and T_{i2} as described in Section 4. The spatial regions are manually chosen to avoid an

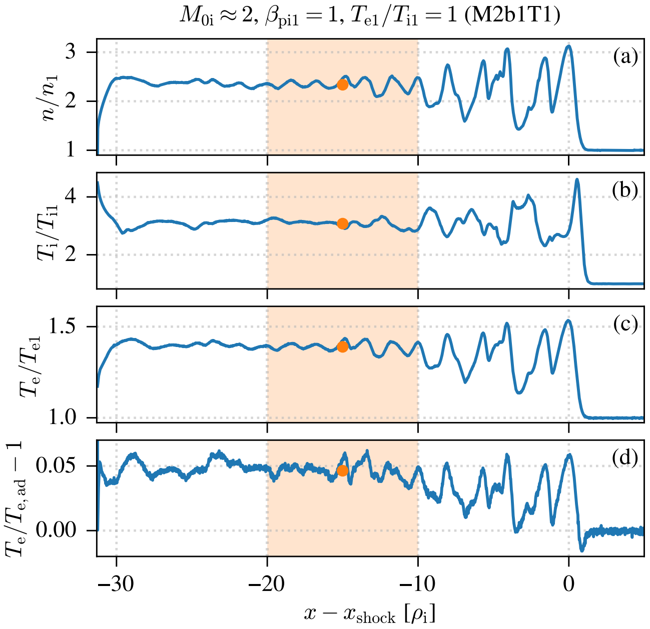

Figure 9. Spatial region $x - x_{\mathrm{shock}} \in [x_{\mathrm{L}}, x_{\mathrm{R}}]$ (orange shaded area) wherein T_{e2} and T_{i2} are measured for the Section 4 analysis, for an example $M_{0\mathrm{i}} \approx 2$, $\beta_{\mathrm{pi1}} = 1$, $T_{\mathrm{e1}}/T_{\mathrm{i1}} = 1$ shock (run M2b1T1.0). From top to bottom, we plot the following y-averaged quantities: (a) rest-frame number density; (b) mean proton temperature; (c) mean electron temperature; (d) excess of electron temperature beyond the adiabatic prediction for an isotropic 3D ultrarelativistic gas; all quantities are defined as in Figures 1–2. The orange markers in panels (a)–(d) show volume averages within the interval [x_{L}, x_{R}].

---

[4] The super/subluminal boundary can equivalently be written as $\cos\theta_{Bn1} = v_1/c$, where θ_{Bn1} is the angle between the upstream magnetic field and shock normal measured in the upstream frame, such that $\tan\theta_{Bn1} = \gamma_1^{-1}\tan\theta'_{Bn1}$ for $\gamma_1 = 1/\sqrt{1 - (v_1/c)^2}$.

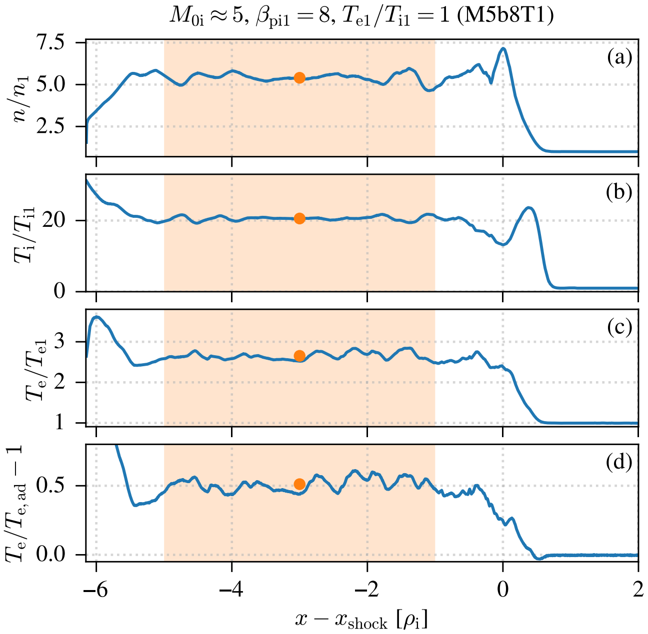

Figure 10. Like Figure 9, but for a $M_{0i} \approx 5$, $\beta_{pi1} = 8$, $T_{e1}/T_{i1} = 1$ shock (run M5b8T1.0).

initialization transient near the left-side wall, and to avoid plasma that has not fully relaxed near the shock front. The displayed shocks show two extremes. At low M_{0i} and low β_{pi1}, shocked downstream plasma takes longer to relax as shock-reflected and energized ions remain gyrophase coherent for multiple Larmor radii behind the shock front (Figure 9). At high M_{0i} and high β_{pi1}, the plasma relaxes quickly, and the downstream measurement region is smaller and closer to the shock in units of ρ_i (Figure 10). In both figures, the full downstream simulation domain is shown. Values for x_L and x_R are given in Table 1 for all simulations.

Appendix C
Simulation Parameters

Table 1 provides simulation input parameters, defined as follows.

1. M_{0i} is the simulation-frame ion-sound Mach number (Section 2).
2. M_s is the measured sonic Mach number (Section 2).
3. $M_A = v_1/v_A$ is the measured Alfvén Mach number, defined using the Alfvén speed $v_A = c\sqrt{\sigma/(1+\sigma)}$, magnetization $\sigma = B_1^2/(4\pi n_1 m_i c^2 h)$, proper upstream magnetic field $B_1 = B_0/\gamma_0$, and other symbols defined in Section 2. Here, h is the specific enthalpy.
4. β_{pi1} is the upstream ion plasma beta (Section 2).
5. T_{e1}/T_{i1} is the upstream electron/ion temperature ratio (Section 2).
6. v_0/c is the simulation-frame upstream plasma flow speed (Section 2).
7. v_1/c is the measured shock speed in the upstream frame (Section 2).
8. $\Omega_i t$ is the simulation time shown in Section 3 and used to measure x_{shock} (Section 2); it is also equal to the selection time $\Omega_i t_{sel}$ for particle-tracing analysis in Section 4.
9. x_{shock} is the shock location at $\Omega_i t$ in units of ρ_i.
10. x_L and x_R define the interval wherein the downstream flow temperatures T_{e2} and T_{i2} are measured (Section 4). Both x_L and x_R are defined as offsets from x_{shock}; both x_L and x_R are reported in units of ρ_i.
11. n/n_1 (taking $n = n_i \approx n_e$) is the proper number density measured as a volume average over the spatial interval $x - x_{shock} \in [x_L, x_R]$.
12. $T_{e2}/T_{e2,ad} - 1$, T_{e2}/T_{e1}, T_{i2}/T_{i1}, and T_{e2}/T_{i2} quantify the postshock ion and electron thermal energy gain, measured as a volume average over the spatial interval $x - x_{shock} \in [x_L, x_R]$ (Section 4).

ORCID iDs

Lorenzo Sironi https://orcid.org/0000-0002-1227-2754
Aaron Tran https://orcid.org/0000-0003-3483-4890

References

Arzamasskiy, L., Kunz, M. W., Chandran, B. D. G., & Quataert, E. 2019, ApJ, 879, 53
Arzamasskiy, L., Kunz, M. W., Squire, J., Quataert, E., & Schekochihin, A. A. 2023, PhRvX, 13, 021014
Begelman, M. C., & Kirk, J. G. 1990, ApJ, 353, 66
Berger, J. M., Newcomb, W. A., Dawson, J. M., et al. 1958, PhFl, 1, 301
Bollimpalli, D. A., Fragile, P. C., Dewberry, J. W., & Kluźniak, W. 2024, MNRAS, 528, 1142
Bollimpalli, D. A., Fragile, P. C., & Kluźniak, W. 2023, MNRAS, 520, L79
Borovsky, J. E. 1986, PhFl, 29, 3245
Buneman, O. 1993, in Computer Space Plasma Physics: Simulation Techniques and Software, ed. H. Matsumoto & Y. Omura (Tokyo: Terra Scientific), 67
Chatterjee, K., Liska, M., Tchekhovskoy, A., & Markoff, S. 2023, arXiv:2311.00432
Comisso, L., & Sironi, L. 2022, ApJL, 936, L27
Conroy, N. S., Bauböck, M., Dhruv, V., et al. 2023, ApJ, 951, 46
Dexter, J., & Fragile, P. C. 2011, ApJ, 730, 36
Dexter, J., & Fragile, P. C. 2013, MNRAS, 432, 2252
Drury, L. O. 1983, RPPh, 46, 973
Event Horizon Telescope Collaboration, Akiyama, K., Alberdi, A., et al. 2019, ApJL, 875, L1
Event Horizon Telescope Collaboration, Akiyama, K., Alberdi, A., et al. 2022a, ApJL, 930, L12
Event Horizon Telescope Collaboration, Akiyama, K., Alberdi, A., et al. 2022b, ApJL, 930, L16
Fairbairn, C. W., & Ogilvie, G. I. 2021, MNRAS, 508, 2426
Fragile, P. C., & Blaes, O. M. 2008, ApJ, 687, 757
Fragile, P. C., Blaes, O. M., Anninos, P., & Salmonson, J. D. 2007, ApJ, 668, 417
Fragile, P. C., Mathews, G. J., & Wilson, J. R. 2001, ApJ, 553, 955
Galishnikova, A., Philippov, A., & Quataert, E. 2023, ApJ, 957, 103
Generozov, A., Blaes, O., Fragile, P. C., & Henisey, K. B. 2014, ApJ, 780, 81
Guo, X., Sironi, L., & Narayan, R. 2017, ApJ, 851, 134
Guo, X., Sironi, L., & Narayan, R. 2018, ApJ, 858, 95
Ha, J.-H., Kim, S., Ryu, D., & Kang, H. 2021, ApJ, 915, 18
Hollweg, J. V. 1985, JGR, 90, 7620
Howes, G. G. 2010, MNRAS, 409, L104
Kaaz, N., Liska, M. T. P., Jacquemin-Ide, J., et al. 2023, ApJ, 955, 72
Kawazura, Y., Barnes, M., & Schekochihin, A. A. 2019, PNAS, 116, 771
Kawazura, Y., Schekochihin, A. A., Barnes, M., et al. 2020, PhRvX, 10, 041050
Kim, S., Ha, J.-H., Ryu, D., & Kang, H. 2021, ApJ, 913, 35
Kirk, J. G., & Heavens, A. F. 1989, MNRAS, 239, 995
Ley, F., Zweibel, E. G., Miller, D., & Riquelme, M. 2024, ApJ, 965, 155
Ley, F., Zweibel, E. G., Riquelme, M., et al. 2023, ApJ, 947, 89
Liska, M. T. P., Kaaz, N., Musoke, G., Tchekhovskoy, A., & Porth, O. 2023, ApJL, 944, L48
McKinney, J. C., Tchekhovskoy, A., & Blandford, R. D. 2013, Sci, 339, 49
Morales Teixeira, D., Fragile, P. C., Zhuravlev, V. V., & Ivanov, P. B. 2014, ApJ, 796, 103
Musoke, G., Liska, M., Porth, O., van der Klis, M., & Ingram, A. 2023, MNRAS, 518, 1656

Narayan, R., & Yi, I. 1995, ApJ, 452, 710
Ogilvie, G. I. 1999, MNRAS, 304, 557
Ogilvie, G. I., & Latter, H. N. 2013, MNRAS, 433, 2403
Raymond, J. C., Ghavamian, P., Bohdan, A., et al. 2023, ApJ, 949, 50
Ressler, S. M., White, C. J., & Quataert, E. 2023, MNRAS, 521, 4277
Rowan, M. E., Sironi, L., & Narayan, R. 2017, ApJ, 850, 29
Rowan, M. E., Sironi, L., & Narayan, R. 2019, ApJ, 873, 2
Spitkovsky, A. 2005, in AIP Conf. Proc. 801, Astrophysical Sources of High Energy Particles and Radiation, ed. T. Bulik, B. Rudak, & G. Madejski (Melville, NY: AIP), 345
Squire, J., Kunz, M. W., Arzamasskiy, L., et al. 2023, JPlPh, 89, 905890417
Tran, A., & Sironi, L. 2020, ApJL, 900, L36
Tran, A., & Sironi, L. 2024, ApJ, 965, 37
Tsokaros, A., Ruiz, M., Shapiro, S. L., & Paschalidis, V. 2022, PhRvD, 106, 104010
White, C. J., Dexter, J., Blaes, O., & Quataert, E. 2020, ApJ, 894, 14
White, C. J., & Quataert, E. 2022, ApJ, 926, 136
White, C. J., Quataert, E., & Blaes, O. 2019, ApJ, 878, 51
Yuan, F., Quataert, E., & Narayan, R. 2003, ApJ, 598, 301
Zhdankin, V. 2021, ApJ, 922, 172
Zhdankin, V., Uzdensky, D. A., Werner, G. R., & Begelman, M. C. 2019, PhRvL, 122, 055101
Zhuravlev, V. V., Ivanov, P. B., Fragile, P. C., & Morales Teixeira, D. 2014, ApJ, 796, 104